Measurement of Attenuation with Airborne and Ground-Based Radar in Convective Storms over Land and Its Microphysical Implications

LIN TIAN

Goddard Earth Science and Technology Center, University of Maryland, Baltimore, Baltimore, Maryland

G. M. HEYMSFIELD

NASA Goddard Space Flight Center, Greenbelt, Maryland

R. C. SRIVASTAVA

University of Chicago, Chicago, Illinois

ABSTRACT

Observations by the airborne X-band Doppler radar (known as EDOP) and the NCAR S-band polarimetric (S-Pol) radar from two field experiments are used to evaluate the surface reference technique (SRT) for measuring the path-integrated attenuation (PIA) and to study attenuation in deep convective storms. The EDOP, flying at an altitude of 20 km, uses a nadir beam and a forward-pointing beam. It is found that over land the surface scattering cross section is highly variable at nadir incidence but is relatively stable at forward incidence. It is concluded that measurement by the forward beam provides a viable technique for measuring PIA using the SRT. Vertical profiles of peak attenuation coefficient are derived in two deep convective storms by the dual-wavelength method. Using the measured Doppler velocity, the reflectivities at the two wavelengths, the differential reflectivity, and the estimated attenuation coefficients, it is shown that supercooled drops and (dry) ice particles probably coexisted above the melting level in regions of updraft and that water-coated partially melted ice particles probably contributed to high attenuation below the melting level.

1. Introduction

Airborne and satellite-borne radars typically operate at wavelengths less than 3 cm to reduce the overall size and weight of the payload and to obtain adequate spatial resolution. The most notable satellite-borne radar is the Tropical Rainfall Measuring Mission precipitation radar (TRMM-PR), which operates at 2.17-cm wavelength (Kummerow et al. 1998). The TRMM-PR estimates rainfall R from radar reflectivity factor Z using empirical Z–R equations. However, at these shorter wavelengths, significant attenuation occurs in storms with heavy rain and wet ice particles, such as melting or water-coated hail or graupel. To estimate the rainfall accurately, it is important to correct for the attenuation. The observation of attenuation can help us to improve algorithms for attenuation correction and thereby the estimation of precipitation by the PR. For a given wavelength and polarization state, the attenuation depends upon the size, concentration, shape, orientation, and composition of the hydrometeors (Battan 1973). In situ microphysical properties are difficult to obtain in high-reflectivity thunderstorm cores. Therefore, the measurement of attenuation can also help us to understand the microphysics of precipitation in such regions.

Three methods have been used to measure attenuation by radar. The dual-wavelength method measures reflectivities at the attenuating wavelength (e.g., 3 cm) and at a nonattenuating wavelength (e.g., 10 cm) simultaneously in a common volume. The difference of the two reflectivity factors[1] gives the two-way path-integrated attenuation (PIA) between the radar and the common volume along the path of the attenuating beam. This method assumes that the wavelength dependence of the backscattering cross sections of the scatterers is accounted for; this can be done for particles in the Rayleigh scattering region (Eccles and Mueller 1971; Meneghini and Kumagai 1994; Bolen and Chandrasekar 2000). The second method, the dual-radar method, utilizes two spaced radars operating at the attenuating

Corresponding author address: Lin Tian, NASA/GSFC, Code 912, Greenbelt, MD 20771.
E-mail: tian@agnes.gsfc.nasa.gov

---

[1] The equivalent reflectivity factor will hereinafter be referred to simply as reflectivity, for the sake of brevity.

TABLE 1. Characteristics of EDOP and S-Pol.

	EDOP	S-Pol
Wavelength (cm)	3.2	10
Beamwidth (°) (circular)	2.9 (nadir and forward)	0.91
Range gate (m)	37.5	150
Antenna gain (dB)	36.1 (nadir), 35.5 (forward)	44.5
Pulse width (μs)	0.5	0.3–1.4
Peak power (kW)	7.6	$<10^3$

wavelength to map the reflectivity field from two aspects. The two reflectivity fields are used to obtain the specific attenuation. This method has been used for airborne radar (Testud and Amayenc 1989) and for ground-based radar (Srivastava and Tian 1996; Tian and Srivastava 1997). The dual-radar method does not require that the scatterers be in the Rayleigh range. The third method uses a reference target of known reflectivity. When a surface target is used as the reference, the method is called the surface reference technique (SRT; e.g., Meneghini et al. 1983). In this method, the reference cross section is first determined by measuring the reflectivity of the ground in a precipitation-free area in close proximity to the precipitating area. When the ground cross section is measured through precipitation, any decrease from the reference cross section is attributed to two-way PIA between the radar and the surface. The SRT is used in processing TRMM-PR data (Iguchi et al. 2000).

The accuracy of the SRT depends upon the stability of the radar cross section of the surface. A number of studies have shown that the ocean surface has a relatively constant cross section. Limited studies have shown that the radar cross section of land can be highly variable, in particular at nadir incidence (Meneghini et al. 2000). A second concern is the change in the surface cross section from wetting and other surface changes accompanying precipitation.

Several field experiments were conducted in support of TRMM. Of interest to us are the Texas and Florida Underflights Experiment-B (TEFLUN-B) held near Melbourne, Florida in August and September of 1998 and the TRMM Land–Biosphere–Atmosphere experiment held in southwestern Amazon in January and February of 1999 (available online at http://www.eosdata.gsfc.nasa.gov/CAMPAIGN.DOC/TRMM-FE). A number of institutions participated in the experiments and deployed a variety of instruments.

In this paper, we present selected instances of high PIA observed over land using an X-band Doppler radar mounted on the National Aeronautics and Space Administration (NASA) ER-2 high-altitude aircraft (EDOP). Nearly simultaneous observations of the thunderstorms were also obtained with a ground-based S-band polarization radar [National Center for Atmospheric Research (NCAR) S-Pol radar] that is not subject to significant attenuation. The characteristics of the radars are listed in Table 1. We shall compare the at-

tenuations derived by the SRT from EDOP observations with those derived by the dual-wavelength method from EDOP and S-Pol observations (sections 3 and 4). We shall interpret the derived attenuations in terms of microphysical properties of the precipitation in section 5.

2. Attenuation observed by EDOP using SRT

a. SRT method

We briefly review the method of obtaining PIA by the SRT and present an example of a storm that shows significant PIA. The observed return power P_s from the surface is related to its normalized radar cross section σ_L^0 by

$$P_s = C_s(\sigma_L^0/r^2) \qquad (1)$$

for nadir incidence and

$$P_s = C_{s1}(\sigma_L^0/r^3)$$

for forward incidence, where C_s and C_{s1} are radar constants (Kozu 1995). The normalized radar cross section σ_R^0 of the surface in the presence of precipitation is related to that in the absence of precipitation, (σ_{NR}^0) by

$$\sigma_R^0 = \sigma_{NR}^0 - A, \qquad (2)$$

where A is the two-way PIA and A, σ_R^0, and σ_{NR}^0 are in decibels. Because σ_{NR}^0 is not measurable, it is replaced by a reference value $\langle\sigma_{NR}^0\rangle$, an average of σ_{NR}^0 for an adjacent rain-free area. Using this reference value, the estimated PIA is

$$\tilde{A} = \langle\sigma_{NR}^0\rangle - \sigma_R^0. \qquad (3)$$

This $\tilde{A}$ can differ from the true PIA, because $\langle\sigma_{NR}^0\rangle$ and σ_{NR}^0 can differ because of changes in surface scattering caused by changes in wind, vegetation, soil moisture, and so on. (Ulaby et al. 1982). We need to know the magnitude of this variability to assess limitations in the measurement of the PIA.

b. Application of SRT to EDOP data

The Doppler radar (EDOP) mounted on the NASA ER-2 aircraft operates at 3-cm wavelength. It has two fixed antennas, one pointing at nadir and the second pointing 33.8° ahead of nadir. The antennas are identical, with a circular beamwidth of 2.9° that defines a footprint at surface of about 1 km at nadir with the assumption that ER-2 flies 20 km above the surface. The ER-2 ground speed is about 210 m s^{-1}, and the integration time for the data processing is 0.5 s. Thus, the surface cross section is oversampled, with one sample being measured every 100 m along the flight track and 10 samples being obtained over one beamwidth. The range resolution of the radar is 37.5 m [for details, see Heymsfield et al. (1996)].

Figure 1a shows a histogram of the surface reflectivity observed by EDOP from the nadir and forward antennas
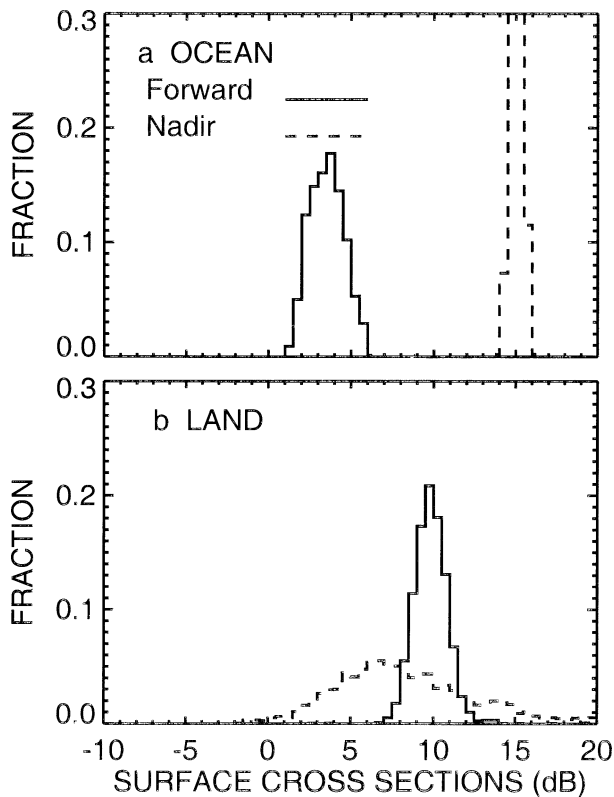
FIG. 1. Histogram of surface scattering cross section over (a) ocean and (b) land at forward (solid) and nadir (dashed) incidence observed by the EDOP radar. Here 20 dB are added to forward surface cross section for display purposes.

for a cloud- and precipitation-free region over the ocean off the Gulf Coast of Florida. The data are typical in that the surface reflectivity of the ocean surface at nadir incidence has small fluctuations of ±1 dB while the echo at 33.8° incidence is more variable, having a standard deviation of about 2 dB. The situation is very different over land (Fig. 1b). At nadir incidence, the reflectivity is highly variable, having a standard deviation of about 4 dB. At forward incidence, however, the surface echo over land shows variability similar to that over the ocean, with a standard deviation of about 2 dB. Distributions such as those in Fig. 1 give limits on the minimum PIA that can be measured and an estimate of error in measured PIA due to surface variability. We see that over land the SRT is subject to larger errors at nadir incidence, whereas at forward incidence PIA can be measured with the same accuracy as over the oceans. This result should be limited to the terrain types observed here, namely, flat areas along the coasts of Florida and Texas, and the Amazon rain forest. For other surfaces and radar observation characteristics, the variability may be different (e.g., Ulaby et al. 1982). We may conclude that, for regions observed by us, the variability of σ^0 over land at 33.8° incidence is about ±2 dB. Therefore, PIA greater than about 2 dB can be mea-

sured over land at 33.8° incidence angle with about the same accuracy.

It is not necessary to measure the absolute value of the surface return, because the SRT is a differential technique. It is important, however, that the surface cross section does not change from wetting by rain, because the SRT will attribute the change to PIA. In the cases studied so far with the EDOP radar, no significant change in surface cross section has been observed at the transitions between rainy and clear conditions for non-nadir incidence.

Figures 2a and 2b show reflectivities observed in a convective cell, embedded in stratiform rain, by EDOP near Ji Parna, Brazil, on 12 February 1999. Figure 2c shows the surface cross section σ^0 measured by the nadir- (dotted) and forward- (solid) pointing beams. In Fig. 2 and subsequent, the reflectivities measured by the forward- and nadir-pointing beams will be denoted as Z_{xf} and Z_{xn}, respectively. Here Z_s will represent the reflectivity measured by the S-Pol radar. All altitudes are above ground level (AGL). The x coordinate is the distance along the flight path from some arbitrary origin; this is the same as the distance along the surface. Note that the forward reflectivity is measured when the radar is ahead of the x coordinate shown in the figure; for the surface observation, it is ahead by 20 km × tan(33.8°), or 13.4 km. The PIA inferred from the forward beam is along a slant path that terminates at the surface at the x coordinate shown.

In Fig. 2a, the nadir-pointing antenna shows a low-reflectivity region near the surface situated below a region of high reflectivity at a distance of about 40 km. The nadir surface cross section σ^0 (Fig. 2c, dotted line) suggests that this low reflectivity is due to attenuation; however, it is difficult to interpret the decrease in σ^0 in terms of PIA with confidence because of the large fluctuations in the background surface cross section at nadir incidence. The reflectivity measured by the forward-pointing antenna (Fig. 2b) is similar to the nadir reflectivity except that a lower reflectivity exists at about 45-km distance, probably due to greater attenuation along the longer slant path of the forward beam. In regions of little or no precipitation, the σ^0 measured by the forward beam (Fig. 2c, solid line) is more stable than that at nadir incidence. The forward minimum σ^0 of −23 dB at 45 km, as compared with the background σ^0 of −8 dB, yields a two-way PIA of 15 dB.

During the two TRMM field campaigns, the ER-2 flew over numerous deep convective storms. The cloud tops, defined by the 10-dBZ contour, reached up to about 13–18 km; many of these storms also showed large PIAs. Table 2 lists eight such cases of storms over land. Most cases have intense convection as indicated by the fact that the 40-dBZ contour reached to 15-km height and the PIA exceeded about 20 dB; such PIA is large for the two-way path of about 20 km. In the following, we present one case from Florida and one from Brazil.
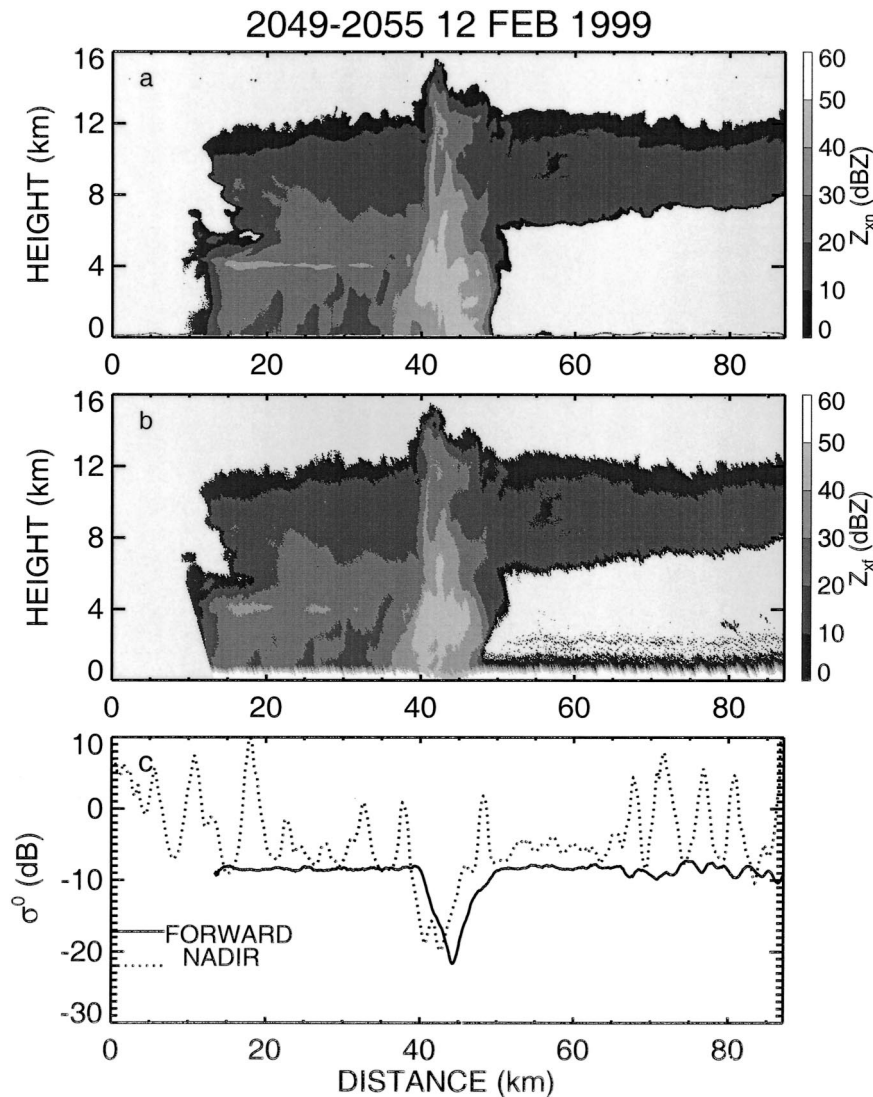
2049-2055 12 FEB 1999

FIG. 2. Vertical cross section of reflectivity at (a) nadir and (b) forward incidence, and (c) surface cross section for forward (solid) and nadir (dashed) beams observed by EDOP radar on 12 Feb 1999 in Ji Parna, Brazil.

These cases were selected because nearly coincident S-Pol observations were also available.

3. Dual-wavelength method and S-Pol data processing

a. Dual-wavelength and k–Z_s methods

The dual-wavelength method takes the difference between S- and X-band reflectivities:

$$Z_s - Z_x = 2 \int_0^r k(r') \, dr' + \delta. \qquad (4)$$

Here k is one-way specific X-band attenuation (no attenuation at S band), and δ is the reflectivity difference due to non-Rayleigh scattering. Figure 3 shows δ for

monodisperse distributions of spherical drops. For diameter less than 2.5 mm, δ can be taken as zero; a minimum δ of about -3.5 dB occurs for diameters of about 6–8 mm.

PIA at 3.2 cm may be estimated using the empirical k–Z_s equation:

$$k = aZ_s^b, \qquad a = 2.9 \times 10^{-4}, \qquad b = 0.72$$

$$(k: \text{dB km}^{-1}, Z: \text{mm}^6 \text{ m}^{-3}), \qquad (5)$$

by integrating $2aZ_s^b$ along the path of the EDOP beam. The above values of a and b are for the modified Marshall–Palmer distribution and spherical raindrops having a temperature of $0°C$ (Battan 1973). The PIAs and attenuations estimated from the above two methods, involving additional S-Pol radar data, are independent of the PIA deduced from the SRT.

TABLE 2. List of EDOP flight legs with PIA larger than 20 dB. The legs indicated by an asterisk are presented in the paper.

Day	Time (UTC)	Location	Max PIA (dB)	Cloud top (km)
*15 Aug 1998	2223–2237	Florida	30	18
5 Sep 1998	2217–2221	Florida	25	16
25 Jan 1999	2215–2223	Brazil	29	16
25 Jan 1999	2242–2246	Brazil	30	16
* 10 Feb 1999	1810–1815	Brazil	29	15
12 Feb 1999	1955–2000	Brazil	20	13
12 Feb 1999	2049–2055	Brazil	15	14
17 Feb 1999	1846–1859	Brazil	23	13

b. S-Pol data processing

The NCAR S-Pol radar operates at 10-cm wavelength, has a beamwidth of 0.91° (circular), and a range resolution of 150 m; it measures Doppler, reflectivity, and polarimetric quantities, such as differential reflectivity (ZDR) and linear depolarization ratio (LDR; for details, information is available online at http://www.atd.ucar.edu).

S-Pol observations were processed as follows. Data from the volume scan nearest in time and space to the ER-2 overflight were interpolated onto a grid in the vertical plane mapped by the EDOP radar. The EDOP has generally higher resolution than S-Pol. At 50-km range, the approximate distance of S-Pol from the storm cases to be discussed, the resolution of the S-Pol beam is 0.87 and 0.15 km in the cross-beam and along-beam directions, respectively; for the EDOP radar, the cross-beam resolution is about 0.76 km at 5-km height and the along-beam resolution is a constant 0.0375 km. S-Pol (and EDOP) reflectivities ($mm^6\ m^{-3}$) were smoothed using the Cressman filter $(R^2 - r^2)/(R^2 + r^2)$, where r is the distance between the observation and interpolation points. Zero weight was assigned to observation points for which r is greater than R. Here R was selected to make the resolutions of the interpolated values nearly equal; R depended upon range from the radar and the radar characteristics. Such smoothing should reduce errors in estimating PIA and attenuation using observations from the different platforms. Still, we can expect errors in regions of high reflectivity gradients, especially near storm boundaries, because of nonuniform and incomplete beam filling. Errors can also be due to temporal displacements. Such displacements were less than 2 min; no attempt was made for time interpolations.

In the next two sections, we present data for the two storms and attempt to 1) validate the attenuation inferred from the SRT and 2) interpret the attenuation in terms of storm microphysics.

4. Case studies of large PIA

a. A storm on 15 August 1998 in Florida

On 15 August 1998, the EDOP observed a 60-km-long N–S line of vigorous convective cells, during
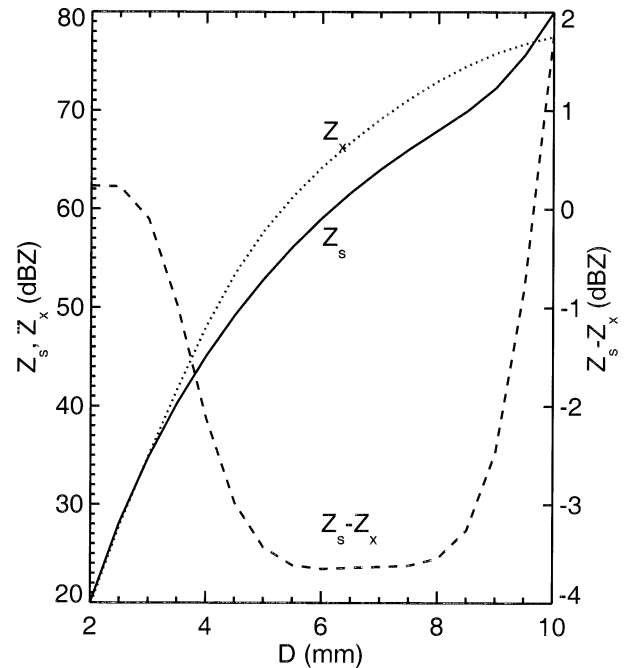

FIG. 3. Reflectivity at S band (solid), X band (short dashes), and their difference (long dashes) for monodisperse distributions of spherical raindrops as a function of drop diameter.

2223–2230 UTC, triggered by the merging of the East and West Coast sea breezes. S-Pol observations, during 2224–2227 UTC, were used to construct Fig. 4, which shows (a) Z_s, (b) ZDR, and (c) LDR at 8-km height. The maximum reflectivity is 58 dBZ about 1 km west of the ER-2 flight line, the projection of which is shown by the solid line. Coincident with the high-reflectivity core, the ZDR is near zero (Fig. 4b) and the LDR is greater than −18 dB (Fig. 4c); this is indicative of wet hail (Doviak and Zrnić 1993).

Figure 5 shows vertical sections of Z_s (Fig. 5a), Z_{xf} (Fig. 5b), the PIA deduced by the SRT (Fig. 5c, solid line), and the PIAs deduced by the two methods outlined above (Fig. 5c, dotted and dashed lines). We see that the 0–10- and 40–50-dBZ Z_s contours reach heights of about 15 and 14 km, respectively, indicating an intense storm. The maximum reflectivities seen by S-Pol and EDOP are 55 and 53 dBZ, respectively (+ in Figs. 5a,b). Such high reflectivities suggest that hail may have been present in the storm.

The maximum PIA measured by the SRT along the forward beam is 25 dB at a distance of about 72 km (Fig. 5c). The PIA obtained by integrating the k–Z_s equation [Eq. (5)] along the forward-pointing beam from storm top to 1-km height (dotted line) has a peak value of about 30 dB. The 5-dB difference between the two peak PIAs exceeds the estimated measurement uncertainty and is probably due to inadequacies in the empirical k–Z_s equation and presence of hydrometeors with characteristics other than those on which Eq. (5) is based.

2224-2227, 15 AUG 1998, Florida
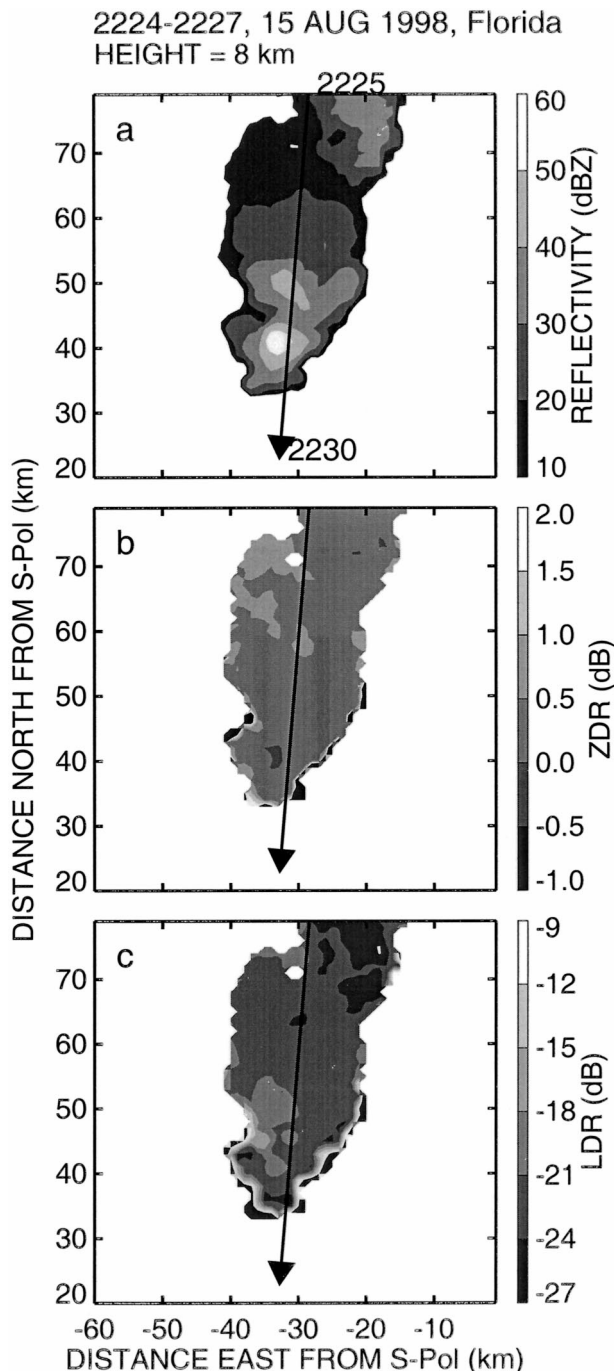### HEIGHT = 8 km

FIG. 4. Constant-altitude, 8-km AGL, contour maps of (a) reflectivity, (b) differential reflectivity (ZDR), and (c) linear depolarization ratio (LDR) in a storm in Florida on 15 Aug 1998, 2224–2227 UTC, reconstructed from S-Pol radar data. The solid line shows the projection of the EDOP flight path.

The PIA deduced from the difference $Z_s - Z_{xf}$ along the forward beam from flight altitude down to a height of 1 km (dashed line) in general is parallel to the other two PIA curves. Its peak value, 28 dB, is in good agreement with the peak PIA from the SRT. This is remark-

able, given that the data came from two radars in different locations and having different resolution volumes. A noticeable difference between the dual-wavelength PIA and the other PIAs is the pronounced dip in the former at a distance of about 74 km. This difference may be due to errors introduced by interpolation performed on the data, especially near storm boudaries. Another possibility is that the dip is due to non-Rayleigh scatterers, such as large hail or raindrops (for the latter, see Fig. 3). To some extent, this conclusion is supported by the fact that, along the slant path, where the beam intersects the dip, there is a pocket of high downward Doppler velocities of about 15–20 m s^{-1} as will be seen later (Fig. 15b, pocket at about 71 km at height of 3–4 km), suggesting large particles and/or strong downdrafts. We favor the idea of large raindrops, rather than hail, because the ZDR values are positive in this region (about 1.5–2.5 dB), as discussed later.

It is also possible to estimate range-resolved PIA by taking the difference $Z_s - Z_{xf}$ at different heights. This procedure would yield attenuation along slant paths. From a microphysical standpoint, vertically resolved PIAs are of greater interest in convective storms; therefore, we shall concentrate on range-resolved attenuation inferred from Z_s and the nadir-beam reflectivity Z_{xn}.

To gain confidence in our data, we first compare the reflectivities measured by the S-Pol and EDOP radars. Figure 6 is a scatterplot of Z_s versus Z_{xn} for the storm in Fig. 5. Except for a relatively small fraction of the points, Z_s and Z_{xn} scatter around the one-to-one line. The standard errors of Z_s and Z_{xn} are estimated to be about 1–2 dB, implying a standard error in $Z_s - Z_{xn}$ of about 1.5–3 dB. This is confirmed by the scatterplots. Therefore, we should be able to measure PIAs greater than 2–3 dB by the dual-wavelength method with a 2–3-dB accuracy. It should be noted that the accuracy of the range-resolved attenuation does not depend upon the absolute accuracy in the measurement of the reflectivities.

Figure 7a is a plot of the S-Pol reflectivities Z_s along the paths of the nadir beam at the heights of 1, 2, 3, 4, 5, and 6 km; in this figure we have not shown reflectivities less than 45 dBZ, because they contribute insignificantly to the PIA. Figure 7b shows dual-wavelength PIAs for the nadir beam from storm top to those heights. Figure 7c shows the corresponding PIAs from integration of the empirical k–Z_s equation. The PIA curves in Figs. 7b,c have similar shapes but differ in magnitude. The main peaks of the PIA in Fig. 7b occur at a distance of about 69 km in the region of highest reflectivities. A second peak occurs at about 75 km in the region of sharp gradient of reflectivity. The PIA in the latter region may not be reliable because of interpolation errors.

b. A storm on 10 February 1999 in Brazil

The EDOP observed a line of convective storms in Brazil during 1811–1816 UTC on 10 February 1999.
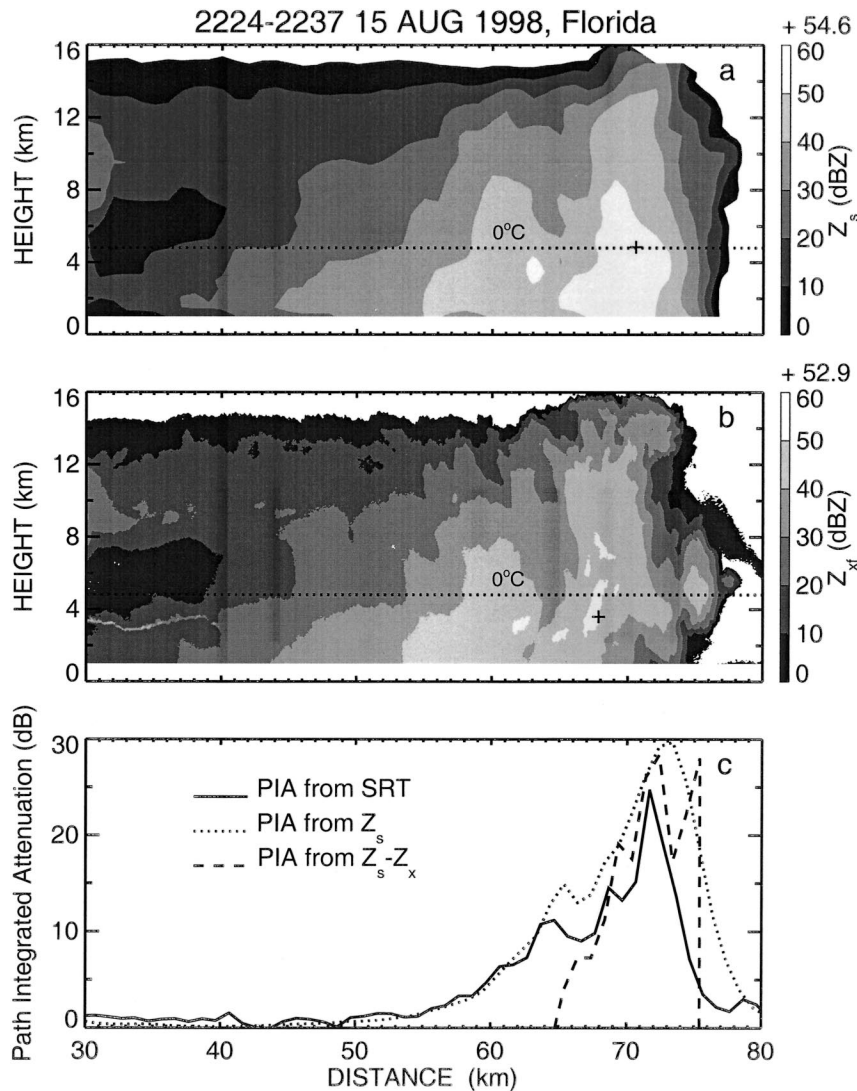
FIG. 5. Vertical cross sections corresponding to Fig. 4 for the Florida storm: (a) reflectivity Z_s from S-Pol radar, (b) forward-beam reflectivity Z_{xf} from EDOP radar, and (c) PIA deduced using the SRT (solid), integration of empirical Eq. (5) (dotted) and the dual-wavelength method (dashed). The 0°C level is indicated by dotted line.

The southernmost cell was located about 50 km north of the S-Pol radar. Figure 8 shows S-Pol reflectivity at 3-km height constructed from the 1810–1815 UTC S-Pol volume scan.

Figure 9a, similar to Fig. 5a, indicates that 0–10- and 40–50-dBZ contours reached heights of about 15 and 7 km, respectively. The maximum reflectivity (+ in Fig. 9a) is 52 dBZ, lower than that in the Florida storm. The maximum reflectivity from the forward beam (Fig. 9b) is only 50 dBZ. We note that the shape of the lower-reflectivity region (Fig. 9b, 30–32 km) tends to align in the direction of the forward beam, a signature of attenuation (Atlas and Banks 1951). The two-way PIA in the direction of the forward beam derived by the SRT (Fig. 9c, solid line) shows a maximum PIA of 29 dB

at a distance of about 32 km. The PIA along the forward path from storm top to 1-km height from the k–Z_s equation (Fig. 9c, dotted line) is similar in shape to the SRT curve but has a peak value of only 12 dB at 32-km distance. The PIA to 1-km height along the forward beam deduced by the dual-wavelength method (Fig. 9c, dashed line) also parallels the SRT, and its peak value, about 19 dB, is also much smaller than the PIA from the SRT. Other discrepancies between the dual-wavelength PIA and the SRT PIA occur mainly in regions of high gradients and at storm edges for reasons already noted.

Figure 10 is a scatterplot of Z_s against Z_{xn}, similar to Fig. 6 for Florida. The points have greater scatter about the one-to-one lines when compared with the Florida
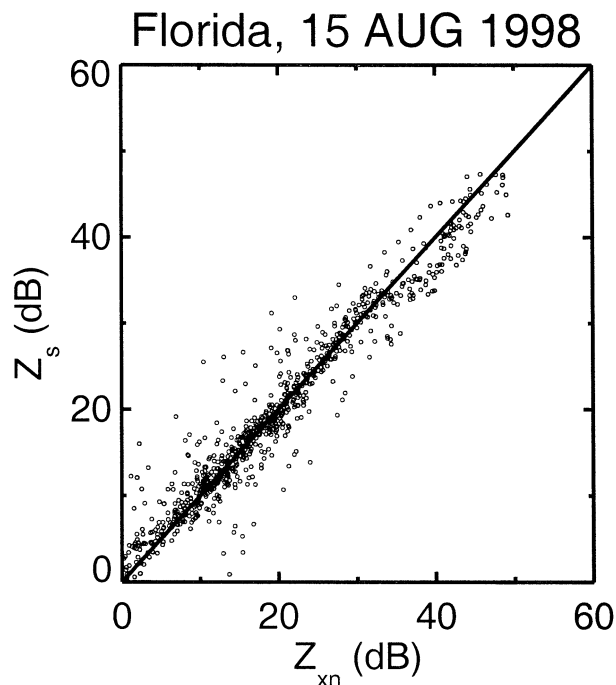
Florida, 15 AUG 1998

FIG. 6. Scatterplot of S-band reflectivity against X-band reflectivities at the nadir incidence for the Florida storm. The one-to-one line is also shown.

FIG. 7. Plots for the Florida storm, for the heights (AGL) of 1.0, 2.0, 3.0, 4.0, 5.0 and 6.0 km: (a) Z_s, (b) difference of S-band and nadir-beam X-band reflectivity $Z_s - Z_{xn}$, and (c) PIA from integration of empirical Eq. (5) along the nadir beam. Vertical line in the plot indicates the distance at which the maximum attenuation occurs. For details see text.

case. One probable reason is that for the Florida case a range–height indicator (RHI) scan was available in close proximity to the EDOP flight plane and time. The Z_s shown was obtained by interpolating the Z_s from the RHI scan to the plane of the EDOP observations. In the case of the Brazil storm a complete volume scan with plan position indicators at different elevation angles was used to construct the vertical plane. The volume scan took about 5 min while the RHI scan was completed in a much shorter time. We believe that the greater time differential between observations by the two radars and a lower density of S-Pol observation points contributed to the greater scatter in the Brazil case.

Figure 11 for the Brazil storm is similar to Fig. 7 for the Florida storm. We again note that the PIA curves derived by the k–Z_s equation (Fig. 11c) and the dual-wavelength method (Fig. 11b) are similar but the former is considerably smaller in magnitude.

The peak two-way PIAs and range-resolved attenuations for the Florida and Brazil storms along vertical paths (solid lines in Fig. 7b and Fig. 11b) are summarized in Tables 3 and 4. (The Z_s and ZDR in the tables were obtained from Figs. 16 and 18 discussed later in section 5b.) In Table 4, there is a negative attenuation in the height interval, 1.5–2.0 km, which is larger in magnitude than the 1.5-dB estimated uncertainty in the dual-wavelength reflectivity ratio. The negative attenuation may be apparent, being the result of larger errors in the reflectivity for the Brazil storm. Another possible reason is the presence of significant con-
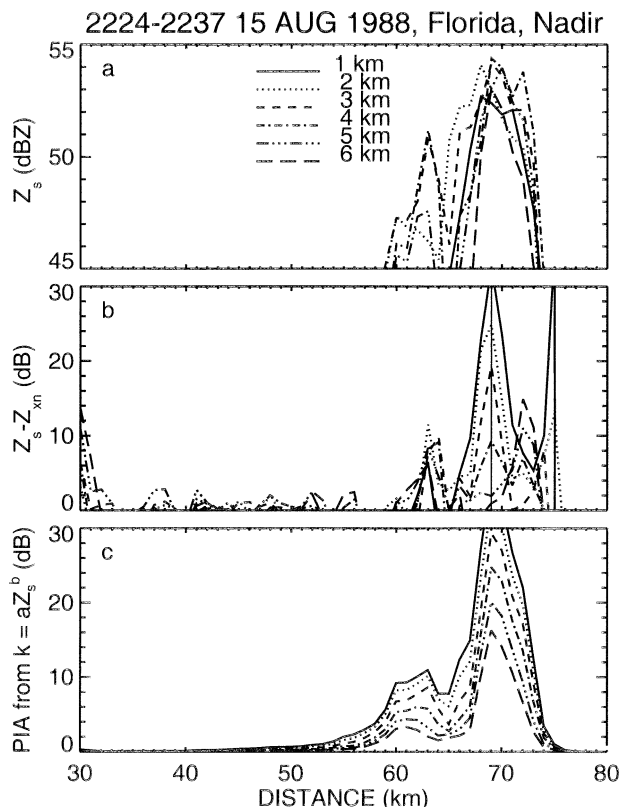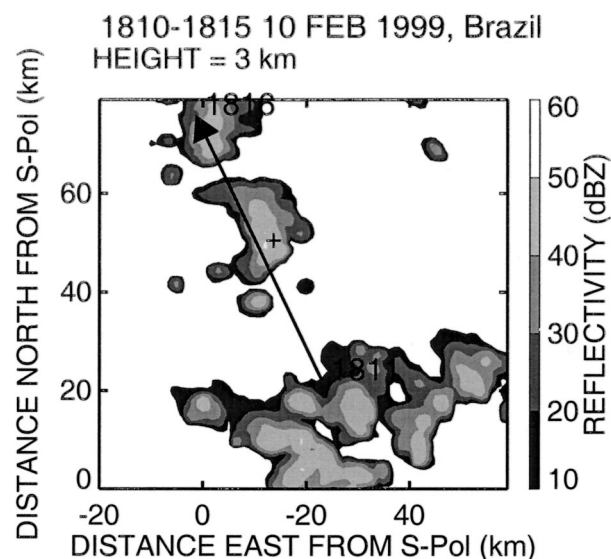

FIG. 8. Constant-altitude, 3-km AGL, contour map of reflectivity for a storm in Brazil on 10 Feb 1999, 1810–1815 UTC, reconstructed from S-Pol radar data. The location of maximum reflectivity is marked by + and the projection of the flight path of the airborne EDOP radar is shown by the line.
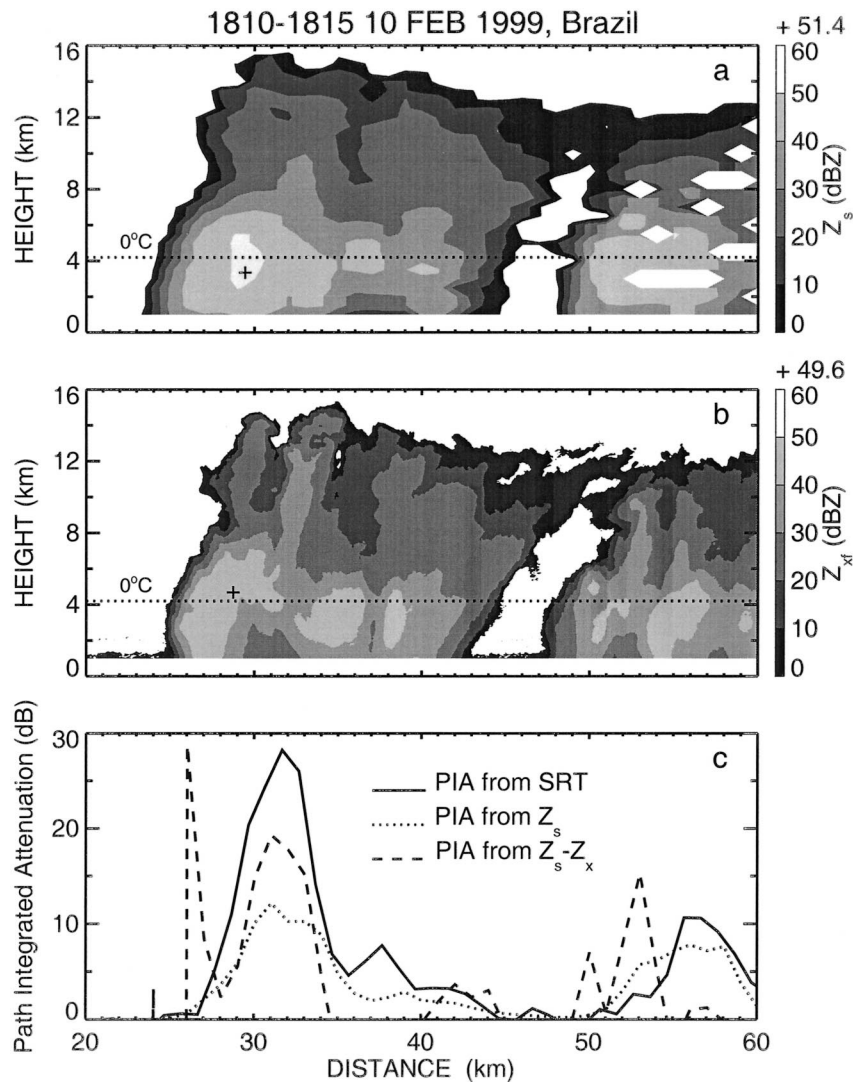
FIG. 9. Similar to Fig. 5, but for the Brazil storm.

centrations of non-Rayleigh scatterers in that height interval.

5. Inferred microphysics from theory and observations

In both the Florida and Brazil storms, the attenuation between the storm top and 5-km height was 1 dB or less (Tables 3, 4). The storm tops, ranging from 10 to 15 km AGL, ensure that ice particles were present in the storm. The small attenuation above 5 km means that this region was dominated by ice particles. As noted before, LDR from S-Pol did suggest presence of wet hail at an altitude of 8 km in the Florida storm, but this was to the west of the flight path of EDOP. Large hail of diameter greater than about 1 cm was probably not present in significant concentrations in the plane of the EDOP observation, because we did not observe any

Mie-scattering effects. Interpretation of the attenuation coefficients inferred for the lower levels is more problematic because raindrops and mixed-phase particles were likely to have been present below the melting level.

In this section, we attempt to interpret the peak attenuations estimated in the lower levels by the dual-wavelength method in terms of the hydrometeors responsible for the attenuation. Because of the great complexity and diversity of the possible distributions of hydrometeors in deep convective storms, and in the absence of in situ observations, our conclusions should be considered as qualitative and preliminary.

To understand better the microphysical processes below the freezing level, we shall also use observations of ZDR by the S-Pol and of the Doppler velocity V_n by the nadir beam of the EDOP radar. Further, we shall use theoretical relationships between reflectivity, attenuation coefficient, and ZDR for gamma function distri-
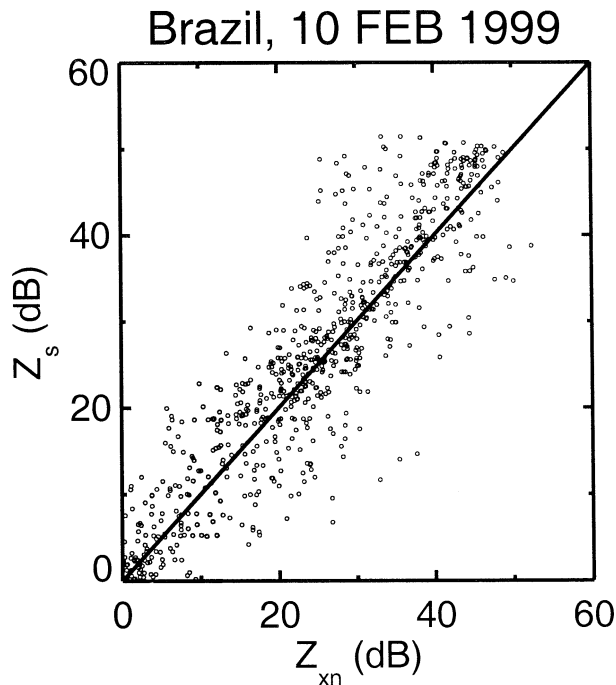
Brazil, 10 FEB 1999

FIG. 10. Similar to Fig. 6, but for the Brazil storm.

FIG. 11. Similar to Fig. 7, but for the Brazil storm.

bution of raindrop sizes as a ''base reference'' case for interpreting the data.

a. Theoretical Relationships

1) ATTENUATION, REFLECTIVITY, AND MEDIAN VOLUME DIAMETER

We assume a gamma raindrop size distribution (Ulbrich 1983):

$$N(D) = N_0 D^\mu \exp(-\Lambda D), \qquad (6)$$

where $N(D)\Delta D$ is the concentration of drops of diameter D to $D + \Delta D$ and N_0, μ, and Λ are parameters of the distribution. For analytical convenience, we assume that the diameter ranges from zero to infinity in Eq. (6), except for the ZDR calculations, for which the maximum diameter is limited to 6 mm. The median volume diameter D_0 is given approximately by

$$D_0 = (3.67 + \mu)/\Lambda. \qquad (7)$$
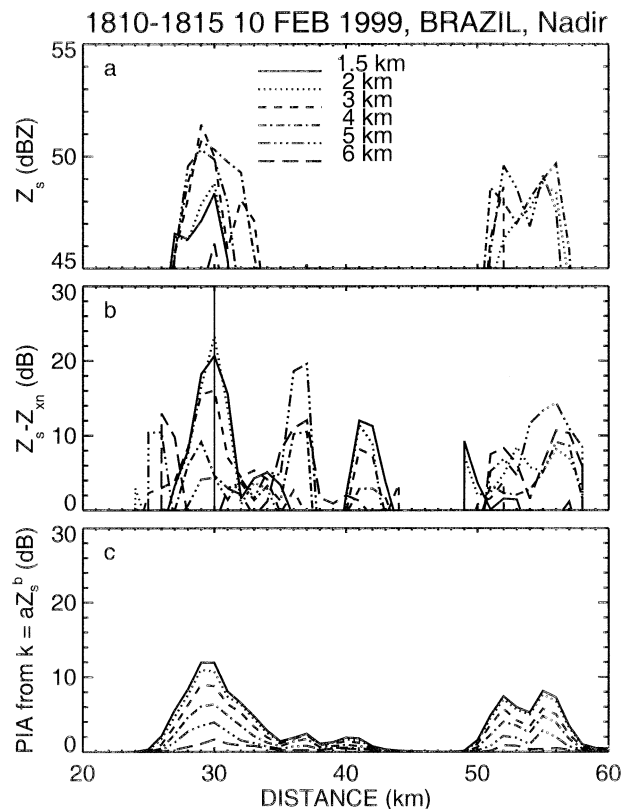
The reflectivity factor is given by

$$Z_s = c_z\left(\frac{N_0}{\Lambda^\mu}\right)\frac{\Gamma(7 + \mu)}{\Lambda^7}. \qquad (8)$$

The extinction cross section of a spherical raindrop can be approximated by a power-law equation (Atlas and Ulbrich 1974):

$$Q_t = aD^n, \qquad (9)$$

where the coefficients a and n depend upon the wavelength and temperature. We shall use numerical values given by Atlas and Ulbrich (see their Table 1); for 3-cm wavelength, $a = 4.18$–13.24 and $n = 4.33$–5.16 for temperatures ranging from 0° to 40°C.

Using Eqs. (6) and (9), the attenuation coefficient is given by

TABLE 3. Summary of inferred attenuation and other parameters for the Florida storm, 15 Aug 1998. The values in the last four columns are for the height intervals in the third column.

Height (km) from top to	Two-way PIA (dB)	Height interval (km)	One-way attenuation (dB km^{-1})	Z_s (dBZ)	ZDR (dB)	Z_s/k
1	33	1–2	4.5	~51	2.5–3.0	2.8×10^4
2	24	2–3	2.5	52–53	2.7–2.5	$(6.3$–$8) \times 10^4$
3	19	3–4	5.0	~52	2.2–2.7	3.2×10^4
4	9	4–5	3.5	~52	1.7–2.2	4.5×10^4
5	2	5–6	0.75	~50–52	1.0–1.7	$(1.3$–$2.1) \times 10^5$
6	0.5	6–top	0.25 dB	~49–51		

TABLE 4. Summary of inferred attenuation and other parameters for the Brazil storm, 10 Feb 1999. The values in the last four columns are for the height intervals in the third column.

Height (km) from top to	Two-way PIA (dB)	Height interval (km)	One-way attenuation (dB km^{-1})	Z_s (dBZ)	ZDR (dB)	Z_s/k
1.5	21					
2	23	1.5–2	−2.0	40–50	1.7–0.8	
3	16	2–3	3.5	~49	1.6–1.7	2.3×10^4
4	6	3–4	5.0	~57	1.6–1.7	2.5×10^4
5	5	4–5	0.5	~51	1.5	2.5×10^5
6	?	5–6	?	~50	1.3–1.5	

$$k = c_k \left(\frac{a}{\Lambda^n}\right)\left(\frac{N_0}{\Lambda^\mu}\right)\frac{\Gamma(n + \mu + 1)}{\Lambda}. \quad (10)$$

From Eqs. (7), (8), and (10) we get

$$\frac{Z_s}{k} = \frac{c_z}{c_k}\frac{\Gamma(7 + \mu)}{\Gamma(n + \mu + 1)}\frac{1}{a}\frac{D_0^{6-n}}{(3.67 + \mu)^{6-n}}. \quad (11)$$

Here, c_z and c_k are numerical constants for unit conversions; their values and the dimensions of the various terms are Z_s: mm^6 m^{-3}, k: dB km^{-1}, $(1/\Lambda)$: cm, (a/Λ^n): cm^2, (N_0/Λ^μ): cm^{-4}, D_0: cm, $N_0 D^\mu$: cm^{-4}, Q_t: cm^2, D: cm, $c_z = 10^{12}$ and $c_k = 4.343 \times 10^5$.

From Eq. (11), we see that given D_0 and μ, Z_s is proportional to k with the proportionality factor depending upon the temperature through a and n. Using Eqs. (7), (8), and (10), we have prepared Fig. 12, which is a plot of k versus Z_s for four temperatures (0°, 10°, 18°, and 40°C), three median volume diameters (1, 2, and 3 mm), and three values of μ (−2, 0, and 4). In preparing Fig. 12, it was not necessary to assume a value of N_0 because, for a given μ and D_0, Z_s determines N_0 [see Eqs. (7) and (8)] and k can then be calculated using Eq. (10). We see from Eq. (11) that, other factors being equal, k increases with temperature because a and n increase with the temperature; this trend is reversed when small drops predominate, that is, for small D_0. We see that, for given Z_s, the median volume diameter D_0 has a pronounced effect on k: a decrease of D_0 results in a significant increase in k. The inferred attenuation coefficients, listed in Tables 3 and 4, are also plotted on Fig. 12. (In this and subsequent figures, the lengths of the bars depict the ranges of reflectivities observed in the height interval and taken from Figs. 16 and 18.)

2) MEDIAN VOLUME DIAMETER AND DIFFERENTIAL REFLECTIVITY

The differential reflectivity (ZDR) is the ratio of the reflectivities at horizontal and vertical polarizations. Raindrop shapes are approximated well by ellipsoids of revolution with their axis ratios being a function of the drop volume. Using equations given in Seliga and Bringi (1976) and the raindrop axis ratio given by Andsager et al. [1999, their Eq. (1)], we have calculated ZDR and plotted it in Fig. 13. We may mention that use of Andsager et al.'s formulation of drop shape is not crucial

for our purposes. Different formulations produce small differences in the calculated ZDR, and we are interested mainly in patterns of variation of ZDR and in diagnosing the presence of liquid drops. The range of median volume diameters plotted is limited by the range of slopes Λ considered to be acceptable, namely, 16–40 cm^{-1}. Note that, unlike Z_s and k, both ZDR and D_0 are independent of N_0. In this figure, we have also indicated the ranges of the observed ZDRs (from Figs. 16 and 18) for the various height intervals for the two storms. Along the horizontal axis, the observed ZDRs have been positioned to intersect the curves for one or more values of μ.

3) REFLECTIVITY FACTOR, ATTENUATION COEFFICIENT, AND DIFFERENTIAL REFLECTIVITY

In Fig. 12, both Z_s and k are proportional to N_0 [Eqs. (8) and (9)], whereas ZDR is independent of N_0. Figure 12 can be used to read off D_0 and μ values that are consistent with the observed Z_s and k. Figure 13 can be used to infer values of D_0 and μ that are consistent with the observed ZDRs. Then, N_0 can be inferred from the observed Z_s. However, Fig. 13 makes use only of the ZDR from the S-Pol radar while Fig. 12 makes use of Z_s and k; inferences from the two figures need not agree. To use all the three measurables, namely, Z_s, k, and ZDR, conveniently and consistently we have constructed Fig. 14, which is a plot of Z_s/k versus ZDR for $\mu = −2$, 0, and 2 and for temperature = 0°, 10°, 18°, and 40°C. Note that Fig. 14 is not independent of Figs. 12 and 13 but is a convenient combination of the two that will facilitate our discussions. In Fig. 14, we have also plotted the observations for the Florida and Brazil storms summarized in Tables 3 and 4.

b. Vertical Doppler velocity and ZDR structure of the storms

Vertical sections of the reflectivities of the two storms have been presented in Figs. 5 and 9. We now present additional observations of the storms to facilitate discussions of the inferred attenuation coefficients.

Figure 15 shows grayshade contour plots of (a) ZDR and (b) V_n, the Doppler velocity measured by the nadir-pointing beam of the EDOP, for the Florida storm. Con-
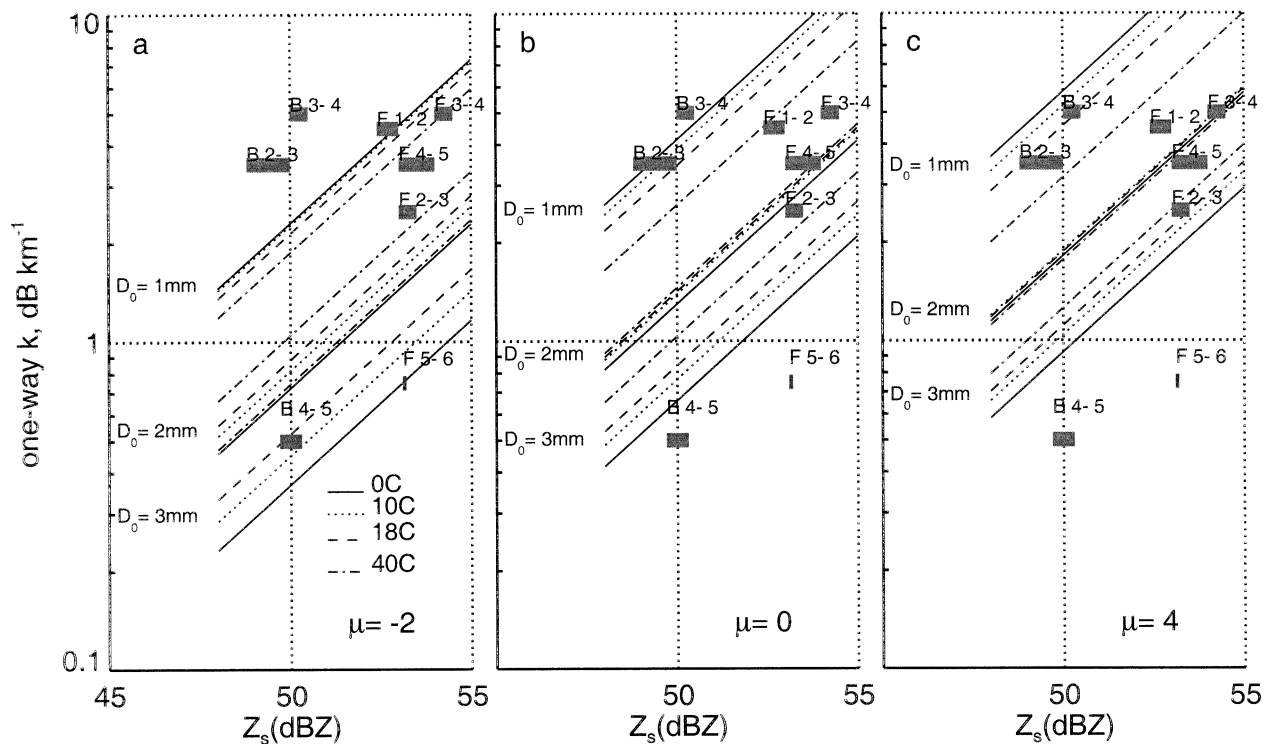
FIG. 12. Specific attenuation at 3-cm wavelength vs reflectivity at 10-cm wavelength for gamma drop size distribution with shape parameters of (a) $\mu = -2$, (b) $\mu = 0$, and (c) $\mu = 4$, for median volume diameters $D_0 = 1$, 2, and 3 mm and temperatures of 0°, 10°, 18°, and 40°C. The inferred specific attenuations and reflectivity along the vertical line in Figs. 7 and 11 for the Florida and Brazil storms are also plotted against reflectivity observed by the S-Pol radar with symbols Fx and Bx, respectively, where x denotes the layer interval in kilometers.
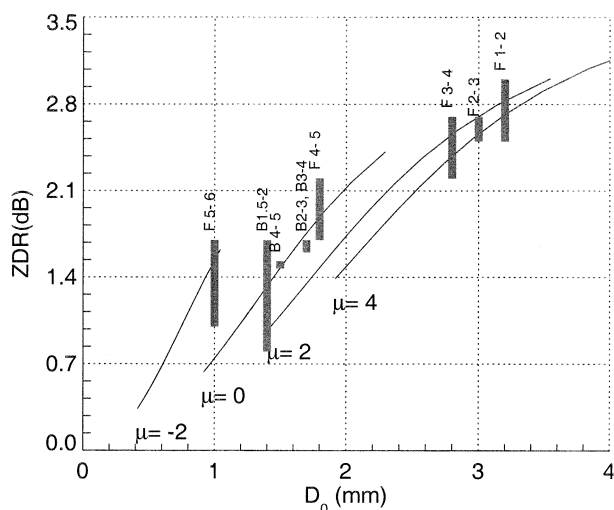

FIG. 13. Differential reflectivity plotted against median volume diameter for $\mu = -2, 0, 2$, and 4 for the gamma drop size distribution. The range of median volume diameters plotted is limited by the range of slopes considered, namely, 16–40 cm^{-1}. Here Fx and Bx specify the Florida and Brazil storms, respectively, where x denotes the layer interval in kilometers. For details, see text.

tours of Z_s have been superposed, and the dashed line shows the locus of maximum V_n. In Fig. 16, we show three vertical profiles of Z_s, Z_{xn}, V_n, and ZDR. The central plot is through the region of peak attenuation and the other two plots are 1 km on either side of it.

Figure 15b shows that this storm has a sloping updraft. A maximum upward V_n of greater than 10 m s^{-1} occurs at a height of about 11 km at 66-km distance. This result implies vertical air velocity of greater than 10 m s^{-1} in that region because V_n is the resultant of the vertical air velocity and the reflectivity-weighted fall velocity of the scatterers. In the vertical profiles we note a regular progression of the region aloft of $V_n > 0$ in going from the left panel to the right panel, a reflection of the sloping updraft. We note that, below the melting level, Z_s is practically constant (central panel, Fig. 16) except in the lowest levels. The ZDR increases downward from about 1.7 dB at the melting level to about 3 dB at the 1-km level (see central panel, Fig. 16; an exception occurs in the 1–2-km height interval in which the ZDR shows a small decrease downward.

Figures 17 and 18 for the Brazil storm are respectively similar to Figs. 15 and 16 for the Florida storm. This storm has a structure similar to that of the Florida storm, but it is weaker as indicated by the reflectivities. The V_n contours again show a well-developed sloping updraft. Upward Doppler velocity of greater than 10 m
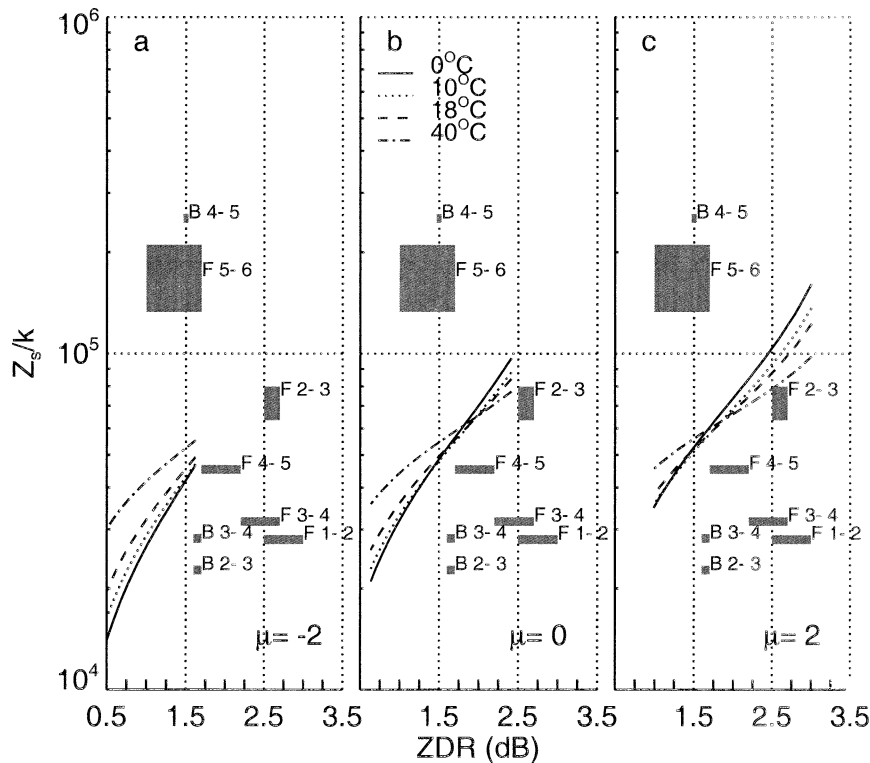
FIG. 14. Plot of Z_s/k vs ZDR for gamma rain DSD for (a) $\mu = -2$, (b) $\mu = 0$, and (c) $\mu = 2$, for four temperatures. The observed "points" are also depicted in the figures. Here Fx and Bx specify the Florida and Brazil storms, respectively, where x denotes the layer interval in kilometers. For details, see text.

s^{-1} occurs at about 10-km height at a distance of 33 km, implying an updraft of greater than 10 m s^{-1}. We see again that, below the melting level, Z_s is practically constant. The ZDRs below the melting level are smaller in this storm as compared with the Florida storm, implying smaller drops in keeping with its weaker reflectivities. In contrast to the Florida storm, the vertical profile of ZDR (central panel) shows that ZDR is practically constant below the melting level (excluding the lowest level, for which the data are questionable).

c. Inferences from the observed Z, ZDR, and k

1) FLORIDA STORM

From Fig. 12, we see that the observed k and Z_s for the 5–6-km height interval (F5–6) could be explained in terms of a gamma rain drop size distribution (DSD) with $\mu = -2$ and a high D_0 of about 3 mm (Fig. 12a). On the other hand, the observed ZDR in Fig. 13 is consistent not only with a rain DSD with $\mu = -2$ and D_0 of about 1 mm, but also with DSDs with $\mu = 0$ and D_0 in the range of 1.2–1.6 mm, $\mu = 2$ and D_0 in the range of 1.4–1.9 mm, and $\mu = 4$ and D_0 in the range of 1.9–2.1 mm. None of these DSD parameters is consistent with $D_0 \approx 3$ mm suggested by Fig. 12. This is evident in Fig. 14 where the observed Z_s/k and ZDR

for F5–6 are not consistent with any gamma DSD considered. The main reason for this inconsistency is that the inferred k is too small for the observed Z_s, giving a large value of Z_s/k. Because this height interval is mostly above the melting level (height 4.8 km), we might conclude that this region was dominated by dry ice particles causing little attenuation. However, the observed ZDRs above the melting level (0.3–1.7 dB in the 5–7-km height interval) imply that raindrops must have been present in that region. This implication is supported microphysically by the strong updraft in the region. Thus, we may conclude that supercooled drops and ice coexisted in this region, with the liquid drops providing the small attenuation and the positive ZDR that was observed.

The next lower height interval, F4–5, has its top near the melting level; therefore, liquid drops and partially melted ice particles may be expected in this region. We see from Fig. 12 that the observed Z_s and k are consistent with a gamma DSD with $\mu = -2$ and D_0 slightly greater than 1 mm (Fig. 12a), $\mu = 0$ and D_0 slightly less than 2 mm (Fig. 12b), and $\mu = 4$ and a D_0 somewhat greater than 2 mm (Fig. 12c). From Fig. 13, we see that the observed ZDR is consistent with DSDs with $\mu = -2$ and $D_0 \approx 1$ mm; $\mu = 0$ and $D_0 \approx 1.6$–2.0 mm; $\mu = 2$ and $D_0 \approx 2$–2.4 mm; and $\mu = 4$ and $D_0 \approx 2.2$–2.6

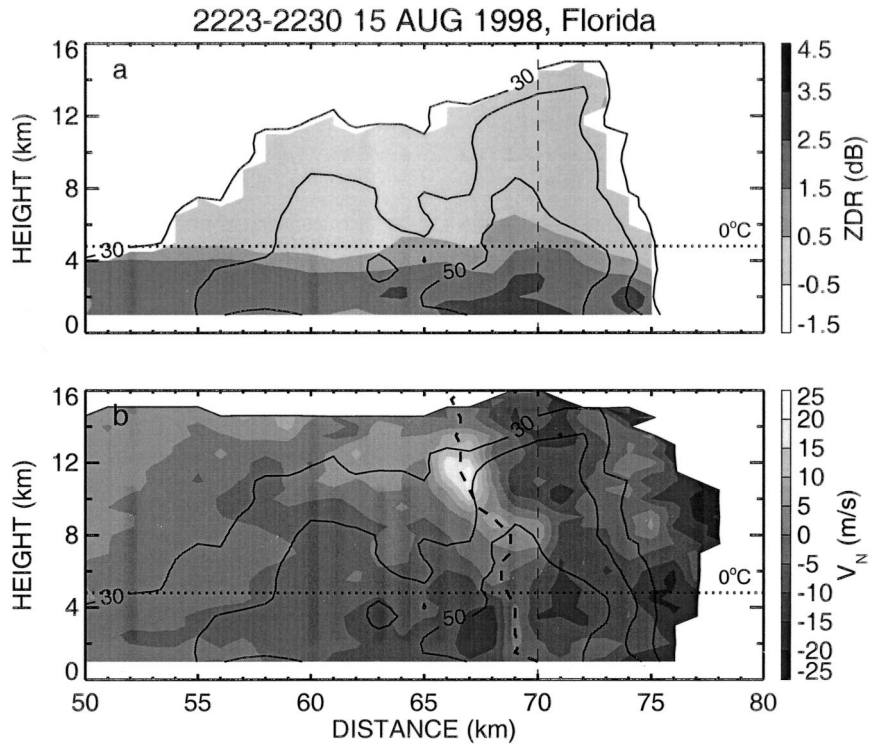## 2223-2230 15 AUG 1998, Florida

FIG. 15. Vertical cross sections of (a) differential reflectivity and (b) nadir-beam Doppler velocity for the Florida storm. S-band reflectivity contours are also shown. The 0°C level is indicated by dotted line. The thin vertical dashed line is the region with maximum attenuation. The thick dashed line is the locus of the maximum updraft.
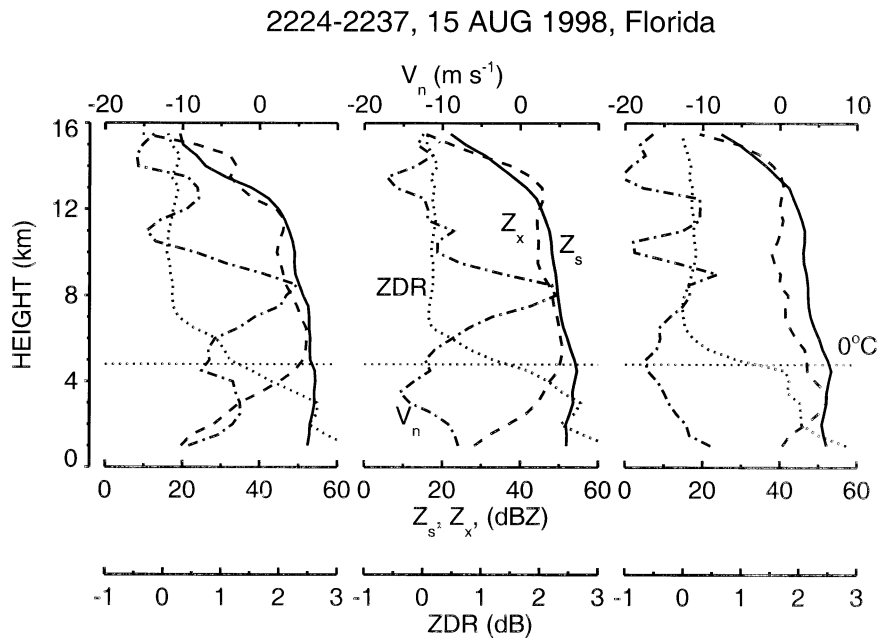
2224-2237, 15 AUG 1998, Florida

FIG. 16. Vertical profiles of S-band reflectivity (solid), X-band nadir-beam reflectivity (dashed), X-band nadir-beam Doppler velocity (dashed–dotted), and differential reflectivity (dotted) for the Florida storm. The central plot is through the region of maximum PIA as indicated by the dashed line in Fig. 15; the left plot is 1 km left of it, and the right plot is 1 km to the right of it.
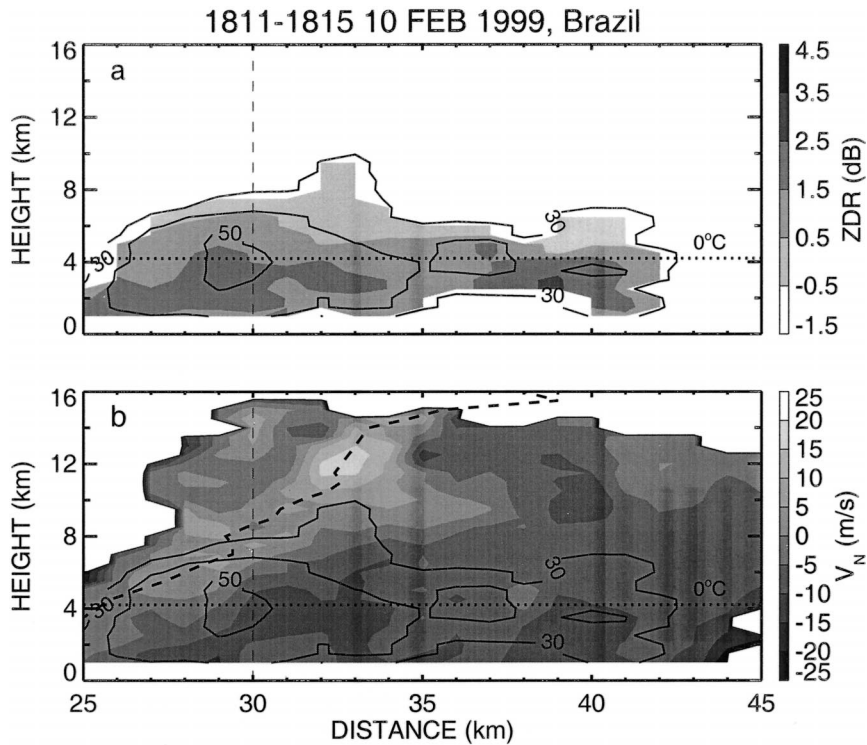
1811–1815 10 FEB 1999, Brazil

FIG. 17. Similar to Fig. 15, but for the Brazil storm.

mm. However, Fig. 14 shows that the observed Z_s/k and ZDR are not consistent with any of the above parameters. This inconsistency is because the k is too high for the observed Z_s, giving a point that lies below the curves in Fig. 14. We conclude that this layer probably contained a mixture of water drops and water-coated ice particles, with the latter providing the high attenuation.

Similar to F4–5, the observed points for F3–4 and F1–2 lie below all the curves in Fig. 14. The attenuation is again too large to be explained by a gamma DSD. We conclude that these regions also contained water-coated melting ice particles that contributed to the high attenuation. Note that if only some of the observables had been considered, for example, only Z_s and ZDR,
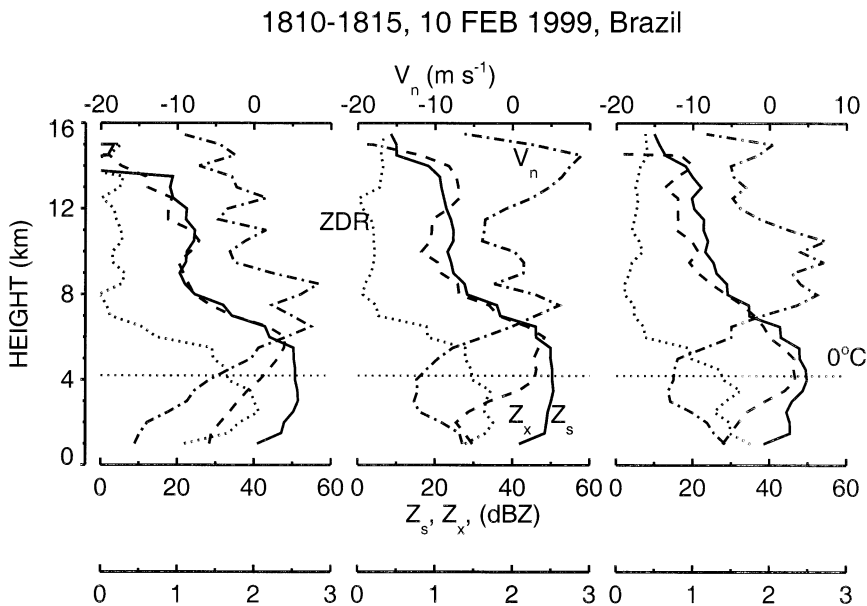
1810–1815, 10 FEB 1999, Brazil

FIG. 18. Similar to Fig. 16, but for the Brazil storm.

then we would have erroneously interpreted the observations in terms of a gamma DSD. The additional information provided by the inferred X-band attenuations strongly suggests that mixed-phase particles were present.

The hypothesis of melting particles is also supported by the systematic increase in ZDR with decreasing altitude as seen in the vertical section and profile of ZDR (Figs. 15 and 16), as well as in Fig. 14. The observed increase in ZDR implies a substantial increase in the mean drop size with decreasing altitude. If only raindrops had been present, the observed increase in mean drop size could not be explained, because the increase of drop size by coalescence is small and is countered by drop breakup. We believe the observed increase in ZDR to be due to the formation of larger drops through the complete melting of progressively larger ice particles with distance fallen. However, this hypothesis needs to be tested through microphysical calculations of the melting of ice particles.

We assumed that water-coated ice particles provided the observed high attenuation. This is supported by earlier work (Battan and Herman 1962). We have calculated the extinction cross section of melting spherical ice particles in which the melt is assumed to form a concentric water coat. This assumption is obviously a simplification, because the coat may be eccentric, the ice core may not be spherical, and the melted water may soak inside the particle, especially in the case of a particle of low bulk density. However, the simplified calculations should provide a qualitative guide. Figure 19 shows the normalized extinction cross section as a function of the fraction of mass melted for several values of the melted diameter and three values of bulk density. The extinction cross section is normalized by the geometric cross section of the melted particle. We see that, for certain sizes and melt fractions, the extinction cross section of the partially melted particle can be several times that of the melted particles. The effect could be larger for deformed particles (Atlas et al. 1953).

2) Brazil storm

The results for this storm are very similar to those for the Florida storm. From Fig. 12, we see that for the 4–5-km height interval (B4–5), which straddles the melting level at 4.2 km AGL, the observed Z_s and k are explainable by a gamma rain DSD with $\mu = -2$ and a large D_0 of about 3 mm (Fig. 12a). This high D_0 is inconsistent with the observed ZDR; according to Fig. 13, the ZDR could be due to gamma DSDs with $\mu = -2$ and $D_0 = 1$ mm, $\mu = 0$ and $D_0 = 1.5$ mm, $\mu = 2$ and $D_0 = 1.8$ mm, and $\mu = 4$ and $D_0 = 2$ mm. This inconsistency between Figs. 12 and 13 is also evident in Fig. 14, which shows that the Z_s/k lies above all the points considered. We again attribute this to a small attenuation because of the predominance of dry ice particles above the melting level. However, the observed
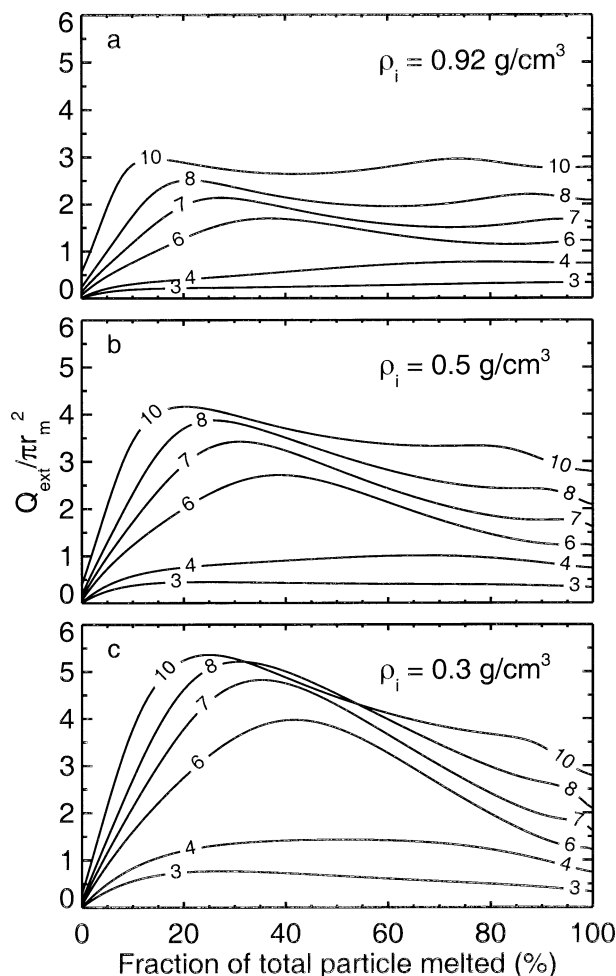

FIG. 19. Normalized extinction cross section of melting ice particles vs fraction of mass melted for selected melted diameters of 3, 4, 6, 7, 8, and 10 mm and three bulk densities of ice: (a) 0.92, (b) 0.5, and (c) 0.3 g cm^{-3}. The ice particle is assumed to be spherical, and melt is assumed to form a concentric sphere coat around it. The normalization is performed by the cross section of the completely melted particle. Calculations are based on Mie theory.

ZDR ($\sim$1.5 dB) again suggests that some supercooled drops were present; these drops would account for the small attenuation that was inferred. Again, the presence of a strong updraft in this region supports the hypothesis of liquid drops above the freezing level. We note the interesting and perhaps significant fact that, for both storms, the points representing the layers immediately above the respective melting levels occupy very similar positions on the diagram of Fig. 14.

The observations for the lower layers, B3–4 and B2–3, are very similar to the observations in the Florida storm below the melting level. Similar to the discussion for the Florida storm, two of the three parameters, Z_s, k, and ZDR, can be used to select the parameters of a gamma DSD to fit the observations. However, Fig. 14 again shows that the Z_s/k points lie below all the gamma DSDs considered. This result implies a k too high for

the observed Z_s to be explained by a gamma DSD. As in the case of the Florida storm, we conclude that liquid drops and partially melted, water-coated ice particles were responsible for the high attenuation.

The ZDR was nearly constant below the melting level in contrast to the Florida storm, which showed a systematic and considerable increase with decreasing altitude. The ZDRs for the Brazil storm are also considerably smaller than for the Florida storm. This result implies that the Brazil storm had smaller particles, which is consistent with the lower intensity of the Brazil storm.

6. Summary and conclusions

Observations by NASA's ER-2 Doppler radar, or EDOP, which operates at 3.2-cm wavelength and makes observations in a nadir- and a 33° forward-pointing beam, show that over land the surface cross section is highly variable at nadir incidence but is stable to within 1–2 dB at the forward incidence. There was no evidence of changes in the surface cross section before entering and after exiting regions of heavy precipitation. Thus, measurement by the forward beam provides a viable method for measuring path-integrated attenuation by the surface reference technique over land. Observations over land in a number of deep convective storms in Florida and Brazil yielded PIAs that exceeded 20 dB between storm top and surface. We selected two storms, one in Brazil and one in Florida, for detailed study using the EDOP and NCAR S-band polarization radar data.

The PIA between storm top and "surface" was also estimated by the dual-wavelength method using the S-Pol (S band) and EDOP (X band) reflectivities. In addition, the dual-wavelength method was used to estimate range-resolved specific attenuation using the S-band radar data and the EDOP radar data from the nadir beam. Very good agreement was found between the forward-beam PIA from the SRT and the dual-wavelength method for the Florida storm; the agreement was not as good for the Brazil storm. The PIA was also calculated by integrating an empirical equation that relates X-band attenuation coefficient and S-band reflectivity for rain. It was found that the PIA so deduced and the PIA found by the SRT had very similar shapes although they differed in magnitude; the two PIAs could probably be made to agree very well by "tuning" the coefficient and exponent in the empirical attenuation–reflectivity equation. However, this tuning procedure has no physical basis as shown by the inferences from the dual-wavelength data and the observed differential reflectivities.

Both storms showed small attenuation above the melting level and significant positive ZDRs in layers a few kilometers thick lying just above the melting level. We concluded that this region was dominated by dry ice particles but had coexisting supercooled drops to account for the observed ZDRs. The Doppler velocity observed by the nadir beam of EDOP also supports the existence of supercooled drops. The Doppler velocities showed strong sloping updrafts extending above the melting level.

Below the melting level, large specific attenuations were deduced by the dual-wavelength method. Theoretical relationships between the attenuation coefficient, reflectivity, and ZDR for a gamma rain DSD were formulated and discussed at length in an attempt to interpret the observations in terms of gamma rain DSD. It was possible to explain the observations in certain height intervals by means of a gamma rain DSD and to deduce its parameters if only two of the three parameters were considered. However, such interpretation was found inconsistent with all three parameters, mainly because the inferred attenuation, below the melting level, was too large for the observed Z_s. We also found a marked and systematic increase in ZDR with decreasing altitude in the Florida storm that cannot be accounted for by the evolution of a rain DSD by coalescence. It was suggested that the large attenuation was due to partially melted water-coated ice particles that present a larger extinction cross section than the completely melted particle. Calculations for spherical water-coated particles showed that the gain in extinction could be very pronounced for melting ice particles of low bulk density. It is also known that deformed particles can cause even more extinction. The Florida storm was more intense than the Brazil storm as suggested by its higher reflectivity. It contained bigger particles, as suggested by larger ZDRs; the larger ice particles required longer fall paths for complete melting and were probably responsible for the observed downward increase of ZDR.

This study has shown the benefits of combining X-band airborne radar observations and S-band polarmetric measurements for the study of microphysics of convective storms. Earlier attempts at using dual-wavelength method for ground-based measurements have used collocated radars or common antennas with matched beamwidths to overcome problems anticipated from lack of coincidence of radar resolution volumes. However, those methods usually yield the attenuation along horizontal paths. For deep convective storms, the structure along a vertical path is of paramount interest. Our study has shown that the combination of a downlooking short-wavelength (Doppler) radar and a ground-based S-band polarimetric radar can be used to infer plausible attenuation coefficients in deep convective storms. Valuable inferences about storm microphysics can be drawn by combining resulting dual-wavelength and ground-based polarimetric data. Such studies are important for improving the SRT over land for future TRMM satellite and to provide a firmer physical basis for its use. With proper design of scan strategies to obtain optimum space–time coincidence between ground-based and airborne radar datasets, it should be possible to obtain more accurate results. The interpretation of dual-wavelength reflectivity, polarimetric, and Doppler velocity observations should be supported by

studies of the characteristics of melting particles, in particular, their radar and extinction cross sections.

REFERENCES

Andsager, K., K. V. Beard, and N. F. Laird, 1999: Laboratory measurements of axis ratios for large raindrops. *J. Atmos. Sci.,* **56,** 2673–2683.

Atlas, D., and H. C. Banks, 1951: The interpretation of microwave reflections from rainfall. *J. Meteor.,* **8,** 271–282.

——, and C. W. Ulbrich, 1974: The physical basis for attenuation–rainfall relationships and the measurement of the rainfall parameters by combined attenuation and rainfall methods. *J. Rech. Atmos.,* **8,** 175–298.

——, M. Kerker, and W. Hitschfeld, 1953: Scattering and attenuation by non-spherical atmospheric particles. *J. Atmos. Terr. Phys.,* **3,** 108–119.

Battan, L., 1973: *Radar Observation of the Atmosphere.* University of Chicago Press, 324 pp.

——, and B. M. Herman, 1962: The radar cross section of ''spongy'' ice spheres. *J. Geophys. Res.,* **67,** 5139–5145.

Bolen, M. S., and V. Chandrasekar, 2000: Quantitative cross validation of space-based and ground-based radar observations. *J. Appl. Meteor.,* **39,** 2071–2079.

Doviak, R. J., and D. S. Zrnić, 1993: *Doppler Radar and Weather Observations.* 2d ed. Academic Press, 565 pp.

Eccles, P. J., and E. A. Mueller, 1971: X-band attenuation and liquid water content estimation by dual-wavelength radar. *J. Appl. Meteor.,* **10,** 1252–1259.

Heymsfield, G. M., and Coauthors, 1996: The EDOP radar system on the high-altitude NASA ER-2 aircraft. *J. Atmos. Oceanic Technol.,* **13,** 795–809.

Iguchi, T., T. Kozu, R. Meneghini, J. Awaka, and K. Okamoto, 2000: Rain-profiling algorithm for the TRMM precipitation radar. *J. Appl. Meteor.,* **39,** 2038–2052.

Kozu, T., 1995: A generalized surface echo radar equation for down-looking pencil beam radar. *IEICE Trans. Comm. Japan,* **E78-B,** 1245–1248.

Kummerow, C., W. Barnes, T. Kozu, J. Shiue, and J. Simpson, 1998: The Tropical Rainfall Measuring Mission (TRMM) sensor package. *J. Atmos. Oceanic Technol.,* **15,** 809–817.

Meneghini, R., and H. Kumagai, 1994: Characteristics of the vertical profiles of dual-frequency, dual-polarization radar data in stratiform rain. *J. Atmos. Oceanic Technol.,* **11,** 701–711.

——, J. Eckerman, and D. Atlas, 1983: Determination of rain rate from a spaceborne radar using measurements of total attenuation. *IEEE Trans. Geosci. Remote Sens.,* **GE-21,** 34–43.

——, T. Iguchi, T. Kozu, L. Liao, K. Okamoto, J. A. Jones, and J. Kwiatkowski, 2000: Use of the surface reference technique for path attenuation estimates from the TRMM precipitation radar. *J. Appl. Meteor.,* **39,** 2053–2070.

Seliga, T. A., and V. N. Bringi, 1976: Potential use of radar differential reflectivity measurements at orthogonal polarizations for measuring precipitations. *J. Appl. Meteor.,* **15,** 69–76.

Srivastava, R. C., and L. Tian, 1996: Attenuation by a dual-radar method: Concept and error analysis. *J. Atmos. Oceanic Technol.,* **13,** 937–947.

Testud, J., and P. Amayenc, 1989: Stereoradar meteorology: A promising technique for observation of precipitation from a mobile platform. *J. Atmos. Oceanic Technol.,* **6,** 89–108.

Tian, L., and R. C. Srivastava, 1997: Measurement of attenuation at C band in a convective storm by a dual-radar method. *J. Atmos. Oceanic Technol.,* **14,** 184–196.

Ulaby, F. T., R. K. Moore, and A. K. Fung, 1982: *Microwave Remote Sensing: Active and Passive.* Vol. 2, Addison-Wesley, 607 pp.

Ulbrich, C. W., 1983: Natural variations in the analytical form of the raindrop size distribution. *J. Climate Appl. Meteor.,* **22,** 1764–1775.